

## **The structure of a propagating $\text{MgAl}_2\text{O}_4/\text{MgO}$ interface: Linked atomic- and $\mu\text{m}$ - scale mechanisms of interface motion**

C. Li<sup>1</sup>, T. Griffiths<sup>1</sup>, T. J. Pennycook<sup>2</sup>, C. Mangler<sup>2</sup>, P. Jeřábek<sup>3</sup>, J. Meyer<sup>2</sup>, G. Habler<sup>1</sup> & R. Abart<sup>1\*</sup>

<sup>1</sup>*Department of Lithospheric Research, University of Vienna, Althanstrasse 14, 1090 Vienna, Austria*

<sup>2</sup>*Faculty of Physics, University of Vienna, Boltzmannngasse 5, 1090 Vienna, Austria*

<sup>3</sup>*Institute of Petrology and Structural Geology, Charles University in Prague, Albertov 6, 12843 Prague, Czech Republic Department*

\*Corresponding author. Email: [rainer.abart@univie.ac.at](mailto:rainer.abart@univie.ac.at)

## The structure of a propagating $\text{MgAl}_2\text{O}_4/\text{MgO}$ interface: Linked atomic- and $\mu\text{m}$ - scale mechanisms of interface motion

To understand how a new phase forms between two reactant layers,  $\text{MgAl}_2\text{O}_4$  (spinel) has been grown between  $\text{MgO}$  (periclase) and  $\text{Al}_2\text{O}_3$  (corundum) single crystals under defined temperature and load. Electron backscatter diffraction data show a topotaxial relationship between the  $\text{MgO}$  reactant and the  $\text{MgAl}_2\text{O}_4$  reaction product. These  $\text{MgAl}_2\text{O}_4$  grains are misoriented from perfect alignment with the  $\text{MgO}$  substrate by  $\sim 2\text{--}4^\circ$ , with misorientation axes concentrated in the interface plane. Further study using atomic resolution scanning transmission electron microscopy shows that in 2D the  $\text{MgAl}_2\text{O}_4/\text{MgO}$  interface has a periodic configuration consisting of curved segments (convex towards  $\text{MgO}$ ) joined by regularly spaced misfit dislocations occurring every  $\sim 4.5\text{ nm}$  ( $\sim 23$  atomic planes). This configuration is observed along the two equivalent  $[100]$  directions parallel to the  $\text{MgAl}_2\text{O}_4/\text{MgO}$  interface, indicating that the 3D geometry of the interface is a grid of convex protrusions of  $\text{MgAl}_2\text{O}_4$  into  $\text{MgO}$ . At each minimum between the protrusions is a misfit dislocation. This geometry results from the coupling between long-range diffusion, which supplies  $\text{Al}^{3+}$  to and removes  $\text{Mg}^{2+}$  from the reaction interface, and interface reaction, in which climb of the misfit dislocations is the rate limiting process. The extra oxygen atoms required for dislocation climb were likely derived from the reactant  $\text{MgO}$ , leaving behind oxygen vacancies that eventually form pores at the interface. The pores are dragged along by the propagating reaction interface, providing additional resistance to interface motion. The pinning effect of the pores leads to doming of the interface on the scale of individual grains.

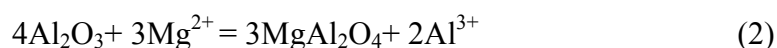
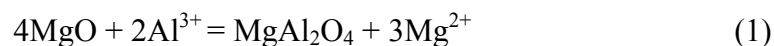
**Keywords:** corundum/spinel/periclase interfacial structures, spinel interlayer growth, atomic structure, HAADF-STEM, EBSD, misfit dislocations, interfaces migration, dislocation climb

### 1. Introduction

In solid-state reactions it is common that a new phase grows as a layer between two materials due to the inter-diffusion of elements between them, this is called interlayer growth. The thickness of the new phase layer is a measurement of the integrated component fluxes and thus depends on the component diffusivities and the reaction time. The layer thickness may only be a few atomic layers for functional materials such as nanomaterials [1,2] or thin film

solar cells [3]. In other applications such as ceramics the new phase may grow much thicker [4]. In natural mineral growth the corresponding phenomenon is referred to as reaction-rim growth or corona formation [5-9]. Understanding the mechanism of interlayer growth is not only important for improving technological material synthesis, but also for reconstructing conditions and rates of mineral growth.

The formation of spinels (general formula  $AB_2O_4$ ) provides an ideal model system for studying the kinetics of layer growth [10]. Experimental growth of spinels in binary systems of  $AO$  and  $B_xO_y$  has been performed in the  $MgO-In_2O_3$  [11],  $MgO-TiO_2$  [4],  $MgO-Al_2O_3$  [12-17], and  $CoO-Al_2O_3$  [10] systems. In this communication we address formation of  $MgAl_2O_4$  spinel (Spl) in the  $MgO-Al_2O_3$  system (Figure 1). This reaction has many practical applications in ceramics and has been studied over more than 60 years [10,16,18,19]. The  $MgAl_2O_4$  interlayer grows in both directions from the original  $MgO$  (periclase, abbreviation Per) –  $Al_2O_3$  (corundum, abbreviation Crn) interface, forming an  $MgAl_2O_4/MgO$  and an  $MgAl_2O_4/Al_2O_3$  reaction interface. At these interfaces reconstructive transformations involving structural and compositional changes occur. As early as 1936, Wagner proposed that inter-layer growth involving ionic crystals may occur by “counter-diffusion” of cations in a stationary anion sub lattice [20]. For the interlayer growth of  $MgAl_2O_4$ , it is generally agreed that  $Al^{3+}$  cations diffuse from  $Al_2O_3$  towards  $MgO$  to propagate the  $MgAl_2O_4/MgO$  interface [17]. Meanwhile  $Mg^{2+}$  cations diffuse from  $MgO$  towards  $Al_2O_3$  to propagate the  $Al_2O_3/MgAl_2O_4$  interface. This process can be described with two equations as below:



Interlayer growth requires two processes to proceed in parallel. Firstly, a layer of a new phase grows and replaces the reactant phases, forming two reaction interfaces, one on each side of

the new layer. The atomic scale processes occurring at the reaction interfaces constitute the *interface reactions*. Secondly, the growth of the new phase also requires the *long-range diffusion* of chemical components across the growing layer, such as the diffusion of  $\text{Al}^{3+}$  and  $\text{Mg}^{2+}$  cations in the  $\text{MgO}/\text{MgAl}_2\text{O}_4/\text{Al}_2\text{O}_3$  system shown above. The overall process including *interface reaction* and *long-range diffusion* is referred to as *reactive diffusion*. The growth rate of the new phase is controlled by the coupling of these two processes, and will be dominated by the slower one. At the early growth stage, diffusion distances are short, and chemical mass transfer by diffusion is very efficient, therefore diffusion is not rate limiting. Instead the interface reaction is usually rate limiting during the early growth stage, which implies linear growth behaviour. Linear growth was indeed documented for spinel layers less than  $\sim 100$  nm thick [14], indicating interface reaction control. With increasing thickness of the new phase, diffusion becomes less efficient and may eventually become rate limiting, resulting in parabolic growth behaviour where layer thickness increases with the square root of time. Parabolic growth has been generally observed in thick layer spinel growth experiments ( $> 1 \mu\text{m}$ ) [13,17,21], suggesting that diffusion control takes over at the later growth stages.

Diffusion controlled layer growth implies local equilibrium at the reaction interfaces. In such a case, the chemical potentials of the components are identical in the two phases on either side of the interface. There is no local thermodynamic force (chemical potential jump across the interface) available to drive interface reaction. For layer growth to proceed in this situation, interface reaction would have to occur without any resistance, i.e. without any kinetic barrier. The intrinsic mobility of the reaction interfaces would have to be infinite. In actual fact, interface reactions are subject to kinetic barriers and proceed at finite rates, so reaction interfaces have finite mobility. This implies that chemical potential jumps do exist at a reaction interface as long as it is moving. Recent research [22] from Abart et al. documented



Al/Mg partitioning that systematically deviated from equilibrium partitioning during spinel layer growth in the MgO-Al<sub>2</sub>O<sub>3</sub> system, testifying to the existence of chemical potential jumps across propagating reaction interfaces. In general, layer growth follows mixed kinetics with both interface reaction and long-range diffusion contributing to overall kinetics. In this context the mechanisms underlying interface motion are important as they ultimately determine the intrinsic interface mobility. To understand the mechanisms of interface motion it is critical to know the local atomic configuration, which is the interface structure.

With the development of modern transmission electron microscopy (TEM), the interface structure of the reaction front can be studied: at the MgAl<sub>2</sub>O<sub>4</sub>/MgO interface periodic misfit dislocations have been found, which are necessary for relaxing the lattice mismatch between MgO and MgAl<sub>2</sub>O<sub>4</sub> [11,19,23]. It has been found that the misfit dislocations may glide or climb depending on the local configuration of misfit dislocations [11,23], while gliding is more energetically feasible [24,25]. Another important finding is that in the MgO-Al<sub>2</sub>O<sub>3</sub> system, a bowed reaction front at the MgAl<sub>2</sub>O<sub>4</sub>/MgO coherent interface is observed, possibly caused by fast and slow movement of different parts of the interface [19]. However, at the time these investigations were made, the resolution of TEM was not good enough to distinguish the exact positions of the misfit dislocation planes at the interface. The dislocation positions were only guessed based on the strain fields derived from the image, and the Burgers vector was guessed to be along  $\langle 110 \rangle$  rather than  $\langle 100 \rangle$  direction.

In order to determine the atomic configuration of the misfit dislocations, we have employed aberration-corrected scanning transmission electron microscopy (STEM) with sub-Å resolution to study the interface structure. The samples studied are MgAl<sub>2</sub>O<sub>4</sub> spinel formed by the reaction of MgO (periclase) and Al<sub>2</sub>O<sub>3</sub> (corundum) crystals at high T (1350°C) by Jeřábek et al. (2014) [15]. The newly formed MgAl<sub>2</sub>O<sub>4</sub> is polycrystalline, bounded by a

MgAl<sub>2</sub>O<sub>4</sub>/MgO interface on one side and by a MgAl<sub>2</sub>O<sub>4</sub>/Al<sub>2</sub>O<sub>3</sub> interface on the other. In this paper we focus on the MgAl<sub>2</sub>O<sub>4</sub>/MgO interface and study its crystallographic orientation relationships, interface geometry and structure at the microscopic and atomic scales. Based on the statistical microscopic results from scanning electron microscopy (SEM) and electron backscatter diffraction (EBSD), interface areas with prominent orientation characteristics were selected, and targeted thin foils were extracted using the focused ion beam technique (FIB) for examination in atomic resolution STEM. Based on these experimental results we discuss the mechanisms underlying the propagation of the MgAl<sub>2</sub>O<sub>4</sub>/MgO interface during MgAl<sub>2</sub>O<sub>4</sub> interlayer growth, and link the interface motion mechanism occurring at the atomic scale with  $\mu\text{m}$  scale interface migration.

## 2. Experiment

Interlayer growth experiments were performed using an uniaxial load apparatus as described in Jeřábek et al. (2014) [15]. Single crystal cuboids of corundum (Al<sub>2</sub>O<sub>3</sub>) and periclase (MgO) with 3×3×5 mm size were assembled together. The [0001] axis of Al<sub>2</sub>O<sub>3</sub> was aligned with one <100> axis of MgO, both axes were perpendicular to the contact surface and both contact surfaces were polished. The experiments were performed in a dry atmosphere maintained by a constant argon gas flow at 0.1 MPa pressure. Uniaxial loading was achieved by applying a constant weight acting perpendicular to the contact surfaces. In this paper, we selected sample No. CP28 from [15], showing a typical MgAl<sub>2</sub>O<sub>4</sub>/MgO interface orientation relationship as revealed by EBSD. The growth conditions for this sample were as follows: the reactants were heated up to 1350° with a 5 °C/min heating rate, and then a 0.261 kN load was applied for 80 hours. After the growth of MgAl<sub>2</sub>O<sub>4</sub>, the samples were cut perpendicular to the crystal contact surfaces in order to prepare a polished thin section for EBSD analysis. The sample preparation procedure was described in more detail by Jeřábek et al. (2014) [15].

An EBSD system equipped on an FEI dual-beam Quanta field emission gun (FEG) scanning

electron microscope (SEM) was used to study the microstructure and the crystallographic orientation relationship between the  $\text{MgAl}_2\text{O}_4$  grains and the reactants. The sample surface was at a working distance of 12 mm, and tilted to achieve a beam incidence angle of  $20^\circ$ . Using a 15 kV accelerating voltage and about 2 nA probe current, EBSD data were collected using the OIM Data Collection software v5.3.1. OIM as well as Matlab with the MTEX toolbox [26,27] was used to analyse the data and export the orientation maps. A focused ion beam (FIB) with Omniprobe<sup>TM</sup> 100.7 micromanipulator, also equipped on the FEI Quanta 3D FEG SEM, was used to extract specimens from the selected interface areas and to thin the specimens to  $\sim 100$  nm thick. A low-kV argon-milling machine was used for final thinning of the specimens to below 50 nm thickness. A Nion UltraSTEM 5<sup>th</sup>-order aberration-corrected STEM with sub-Å resolution was employed to resolve the atomic structure of the interface using 100 kV accelerating voltage. A high angle annular dark field (HAADF) detector was used to obtain most images, the signal from which is a ratio of the square of atomic numbers (so called Z-contrast images). The probe-forming angle and the inner detector angle for the Z-contrast images were approximately 30 and 80 mrad respectively.

### 3. Results

#### 3.1 Orientation relationship from EBSD

The EBSD inverse pole figure (IPF) map in Figure 2 uses different colors to indicate different orientations. It shows that the  $\text{MgAl}_2\text{O}_4$  spinel layer splits into two different orientations: a thinner part of the layer has a crystallographic orientation relation (COR) with MgO (Per-ori Spl), whereas a thicker part of the layer has a COR with  $\text{Al}_2\text{O}_3$  (Crn-ori Spl).

In the Crn-ori Spl layer, the grains have equivalent twin orientations which relate to one another by a  $60^\circ$  rotation round [111] (dark green and light green in the IPF map). The  $\text{MgAl}_2\text{O}_4$  grains in both twin orientations show a “topotaxial” orientation relationship (in which the precursor material determines the orientation of the product) with the  $\text{Al}_2\text{O}_3$

corundum substrate:  $(111)_{\text{spl}} \parallel (0001)_{\text{crn}}$  and  $\{101\}_{\text{spl}} \parallel \{10\text{-}10\}_{\text{crn}}$ . In the Per-ori Spl layer (red in the IPF map),  $\text{MgAl}_2\text{O}_4$  spinel grains show a topotaxial orientation relationship with the MgO periclase substrate (also red in the IPF map due to its identical orientation):  $\{001\}_{\text{spl}} \parallel \{001\}_{\text{per}}$ . These features are consistent with the previous results [18], and are typical for most of the  $\text{MgAl}_2\text{O}_4$  samples grown under different load, temperature and duration time by Jeřábek et al. (2014).

Further investigation of the EBSD data revealed new details about the crystallographic orientation relationship between the MgO reactant and Per-ori Spl layer not discussed by Jeřábek et al. (2014). To describe these relationships, we must first clarify how we chose to label the different symmetrically equivalent  $\langle 100 \rangle$  directions of MgO and  $\text{MgAl}_2\text{O}_4$ . As these directions are equivalent the choice of which direction to specify as  $[100]$  is arbitrary. In this paper, we label the MgO directions as follows:  $[100]$  in the interface, subparallel to the  $x$  direction in maps,  $[010]$  in the interface, subperpendicular to the plane of the map, and  $[001]$  perpendicular to the interface, subparallel to the  $y$  direction in maps. As the Per-ori Spl is topotactic to the MgO, the same naming convention is extended to these grains, i.e. Per-ori Spl direction  $[100]$  is subparallel to MgO  $[100]$ .

Figures 3 (a-c) illustrate the new observations using a section from a larger map, however the relationships described were found to be the same for all Per-ori Spl grains grown into MgO. Each map illustrates the misorientation angle between one MgO  $\langle 100 \rangle$  direction (see legend at right) and the corresponding  $\text{MgAl}_2\text{O}_4$   $\langle 100 \rangle$  direction. Colors from dark to white indicate misorientation angles from  $0^\circ$  to  $4^\circ$ .

The  $[001]$  direction of the MgO reactant (perpendicular to the interface) is almost never parallel to  $\text{MgAl}_2\text{O}_4$   $[001]$  in the Per-ori Spl layer. The deviation usually ranges from  $2\text{-}4^\circ$  (Figure 3 (c)). Deviations from in-interface MgO directions range from  $0\text{-}4^\circ$ , where small

deviation from one in-interface MgO  $\langle 100 \rangle$  direction correlates with larger deviation from the other (Figure 3 (a-b)). The same trend is shown for an entire map's Per-ori Spl data points in the corresponding inverse pole figure (IPF) plots in Figure 3 (d-f). All these observations are consistent with the fact that the misorientation axes between MgO and  $\text{MgAl}_2\text{O}_4$  are concentrated in the interface plane (Figure 3g). Given the low precision of misorientation axis determination for standard EBSD ( $\pm 18^\circ$  for a misorientation angle of  $3^\circ$  and an EBSD orientation precision of  $\pm 1^\circ$ ) the exact location of maxima within this plane cannot be determined, but there does seem to be a slight concentration near to in-interface MgO  $\langle 100 \rangle$  directions.

In the EBSD maps, some grains show one of the  $[100]$  and  $[010]$  directions nearly parallel with the corresponding direction in the MgO substrate. In Figure 3, red and blue arrows are used to mark out the  $\text{MgAl}_2\text{O}_4$  grains (and sub-grains) with  $[100]$  or  $[010]$  directions parallel to the corresponding axes in MgO, respectively. The FIB specimen was extracted from one area with this typical orientation relationship marked by the black boxes in Figure 3 and further thinned to  $\sim 50$  nm thickness. The size of the  $\text{MgAl}_2\text{O}_4$  (sub)grains is 1-4  $\mu\text{m}$  along the  $[100]$  axis, therefore the FIB specimen (length parallel to  $[010]$  axis  $\sim 14$   $\mu\text{m}$ ) is expected to contain a few  $\text{MgAl}_2\text{O}_4$  grains with small orientation variations.

### ***3.2 Voids at the topotaxial $\text{MgAl}_2\text{O}_4/\text{MgO}$ interface and domed interface at $\mu\text{m}$ -scale***

Another finding on the interface is that there are voids at the  $\text{MgAl}_2\text{O}_4/\text{MgO}$  interface (Figure 4), but only in the topotaxial part. The crn-ori Spl occasionally reaches the MgO substrate, forming presumably incoherent  $\text{MgAl}_2\text{O}_4/\text{MgO}$  interface segments where voids are absent (the black box in Figure 4(b)).

Similar voids have also been found in the extracted FIB specimen. The STEM HAADF images in Figure 5 show an overview of the entire specimen, the viewing direction is

perpendicular to the foil marked in Figure 3, close to the [100] direction in the MgO substrate. The foil comprises 8 (sub)grains showing several characteristic features. Firstly, the pores are mostly located at the junctions of the  $\text{MgAl}_2\text{O}_4/\text{MgO}$  interface and grain boundaries (GBs). The pores are definitely not artefacts from sample preparation under the ion-beam, because the SEM and EBSD images of bulk samples also show characteristic pores at the  $\text{MgAl}_2\text{O}_4/\text{MgO}$  interface (Figure 4). Secondly, the  $\text{MgAl}_2\text{O}_4$  grains are elongated approximately perpendicular to the  $\text{MgAl}_2\text{O}_4/\text{MgO}$  interface. Thirdly, the interface is not planar at the  $\mu\text{m}$ -scale from grain to grain:  $\text{MgAl}_2\text{O}_4$  grains protrude into MgO with a domed shape, convex towards MgO.

### ***3.3 Atomic interface configuration by STEM: nm-scale scalloped interface with periodic misfit dislocations***

After zooming in to the  $\text{MgAl}_2\text{O}_4/\text{MgO}$  interface at the top of one of the  $\mu\text{m}$ -scale  $\text{MgAl}_2\text{O}_4$  domes (location marked as Figure 6 in Figure 5), a periodic interface with a “scallop” shape consisting of curved interface segments (convex towards MgO) is observed. Between the curved interface segments, the interface forms cusps pointing towards  $\text{MgAl}_2\text{O}_4$ , as shown in Figure 6 (a). The spacing between cusps is  $\sim 4\text{nm}$ . The atomic STEM image in Figure 6 (b) shows that the (010) planes of the  $\text{MgAl}_2\text{O}_4$  grain are tilted less than  $0.6^\circ$  from the corresponding (010) planes of the MgO substrate. However, when this  $\text{MgAl}_2\text{O}_4$  grain is tilted to exactly the [100] zone axis, the MgO substrate does not show atomic structure but only planes. Therefore the  $\text{MgAl}_2\text{O}_4$  grain is tilted away from the MgO substrate around the [010] axis and only the (010) planes of  $\text{MgAl}_2\text{O}_4$  and MgO are close to perfect alignment. This is consistent with the EBSD result in Figure 3. The orientation relationship is sketched in Figure 6(c).

Another important feature is that there are misfit dislocations at the interface  $\sim 23$  planes ( $\sim 4.5\text{ nm}$ ) apart from each other. The extra  $\text{MgAl}_2\text{O}_4$  planes are marked by red boxes in Figure

6(b). The spacing between the misfit dislocations is very consistent for the flat interface fronts, such as the area shown in Figure 6 (a). Furthermore, the misfit dislocations are always at (or near) the cusps positions on the interface.

An interface section between another  $\text{MgAl}_2\text{O}_4$  grain and the MgO substrate (location marked as Figure 7 in Figure 5) is shown in Figure 7. This  $\text{MgAl}_2\text{O}_4$  grain has a slightly different orientation to the grain in Figure 6. The atomic columns are visible in both MgO and  $\text{MgAl}_2\text{O}_4$  in the Z-contrast image in Figure 7 (a), indicating that both  $\text{MgAl}_2\text{O}_4$  and MgO are being viewed along their [100] zone axis. In the atomic STEM Z-contrast images, the difference between  $\text{MgAl}_2\text{O}_4$  and MgO is obvious: there are interstitial atoms in the cubic lattices in  $\text{MgAl}_2\text{O}_4$  while not in MgO. At the current projection along the [100] zone axis, the angle between the [001] directions of MgO and  $\text{MgAl}_2\text{O}_4$  is about  $1.9^\circ$ , and the angle between their [010] directions is about  $2^\circ$ . This shows that the  $\text{MgAl}_2\text{O}_4$  grain has rotated by about  $\sim 2^\circ$  away from the MgO lattice around the [100] direction, which is again consistent with the EBSD results in Figure 3. The orientation relationship is drawn by the sketch image in Figure 7(b).

Although the  $\text{MgAl}_2\text{O}_4/\text{MgO}$  orientation relationship shown in Figure 7 is different from the one in Figure 6, the interface shows a similar periodic scalloped-shape, with a  $\sim 4.5$  nm spacing between cusps on the interface. There are also misfit dislocations at the cusps position, where the red boxes meet the interface in Figure 6(a), which are about 20-23 planes (4-4.5 nm) apart from each other. Since the configuration in Figure 7(b) can be considered identical to the situation in Figure 6(c) with a  $90^\circ$  rotation around [001], these results can be used to build a 3D interface configuration which will be discussed in section 4.1.

Figure 6 shows the atomic structure at the flattest interface section, near the head of one  $\mu\text{m}$ -scale domed reaction front protrusion. The area of Figure 7 is located at a weakly curved interface section. Figure 8 shows the interface structure at a much more inclined area at the

side of a domed  $\text{MgAl}_2\text{O}_4$  grain protrusion, the position of which is marked in Figure 5. The atomic structure again shows a periodic scalloped-shape configuration at the interface, with the presence of misfit dislocations. At these inclined interface sections at the edges of  $\mu\text{m}$ -scale  $\text{MgAl}_2\text{O}_4$  protrusions, the average spacing between the dislocations is shorter compared to the flatter interface sections (Figures 6-7). Furthermore, the “scalloped-shape” feature at this part of the interface is more fuzzy, but still visible. The possible reasons for this will also be discussed in section 4.1.

## 4. Discussion

### *4.1 Interface 3D model: supercells formed with periodic nm-scale $\text{MgAl}_2\text{O}_4$ convex segments and misfit dislocations*

From the STEM observations we can infer a schematic model for the  $\text{MgAl}_2\text{O}_4/\text{MgO}$  interface structure. Figure 9 (a) is a 2D sketch showing a single misfit dislocation in  $\text{MgAl}_2\text{O}_4$  at one cusp of the scalloped-shape interface (the extra  $\text{MgAl}_2\text{O}_4$  plane is shown in the red box).

The misfit dislocations observed in STEM images are the projection of extra  $\text{MgAl}_2\text{O}_4$  planes that are parallel to the beam direction. Combining the STEM results from Figures 6 and 7, equivalent to a similar structure with a  $90^\circ$  rotation, a 3D interface configuration can be drawn, as shown in Figure 9 (b). The interface surface has a periodic hill-shape in 3D. The red planes underneath indicate the extra planes in  $\text{MgAl}_2\text{O}_4$ , forming misfit dislocations where they intersect the phase boundary. The misfit dislocations together with the periodic curved interface surface form supercells, which have a lattice parameter of  $\sim 4.5$  nm in both  $[100]$  and  $[010]$  directions. The detailed structure of the points where four supercells intersect is demonstrated in Figure 9 (c), showing that three  $\text{MgAl}_2\text{O}_4$  planes merge into two  $\text{MgO}$  planes along both  $[100]$  and  $[010]$  directions (red planes indicate extra  $\text{MgAl}_2\text{O}_4$  planes). Note this is



a simplified model that does not consider the association of different dislocations. Similar supercell configurations have been predicted based on atomistic simulations of a SrTiO<sub>3</sub>/MgO interface, which is considered to be a flat 2D configuration [28].

The array of misfit dislocations can be well understood in terms of the O-lattice (note: not oxygen lattice) model [29]. The O-lattice is a purely geometrical concept based on the notion that in two interpenetrating crystal lattices, a 3D periodic array of points that have identical coordinates in the unit cells of both crystal lattices can be found. Half way between the O-lattice points, the largest possible misfit between the two interpenetrating lattices occurs. MgO and MgAl<sub>2</sub>O<sub>4</sub> both have a face-centered cubic (fcc) oxygen sublattice with similar lattice spacings. For MgO, the lattice parameter  $a_{\text{MgO}} = 4.217 \text{ \AA}$ . For MgAl<sub>2</sub>O<sub>4</sub>, the lattice parameter  $a_{\text{MgAl}_2\text{O}_4} = 8.080 \text{ \AA}$  and the lattice parameter for its fcc oxygen sublattice is exactly half this value. For the sake of simplicity, we disregard the 2° angular misfit and consider MgAl<sub>2</sub>O<sub>4</sub> and MgO to have same orientation. In this case the O-lattice is cubic, with lattice vectors parallel to the lattice vectors of the two cubic crystals. Therefore the lattice misfit at the MgAl<sub>2</sub>O<sub>4</sub> /MgO interface is  $2 \frac{a_{\text{MgAl}_2\text{O}_4} - 2a_{\text{MgO}}}{a_{\text{MgAl}_2\text{O}_4} + 2a_{\text{MgO}}} \approx -4.3\%$  in both the [100] and [010] directions. A perfect lattice match is calculated to occur after every ~23 lattice planes. The locations of maximum mismatch are represented by a set of three mutually perpendicular planes with orientations (100), (010) and (001), corresponding to the locations where misfit dislocations are most likely to occur. This is in perfect agreement with our observations of the geometry of misfit dislocations at the interface, given that for an interface parallel to MgO (001) no misfit needs to be accommodated in the [001] direction.

The smaller spacing of misfit dislocations on the inclined flanks of  $\mu\text{m}$ -scale domed MgAl<sub>2</sub>O<sub>4</sub> protrusions into MgO (Figure 8) might be caused by increased strain from the domed surface. Meanwhile at the inclined slopes, misfit dislocations not only exist along [100] and [010]

directions on (001) planes, but also along the [001] direction. This is likely the reason for the more blurry and less pronounced scalloped-shape interface structure on the flanks of protrusions compared to the frontal, less curved interface sections.

#### ***4.2 Kinetic balance: formation of the scalloped-shape interface on the nm-scale—The diffusion of O, Mg and Al atoms during the formation of $\text{MgAl}_2\text{O}_4$***

In the interface sections between the misfit dislocations, the MgO and  $\text{MgAl}_2\text{O}_4$  lattices are perfectly aligned at the interface plane. The growth of  $\text{MgAl}_2\text{O}_4$  into MgO is driven by the continuous supply of  $\text{Al}^{3+}$  cations liberated at the  $\text{Al}_2\text{O}_3$ - $\text{MgAl}_2\text{O}_4$  interface and delivered to the  $\text{MgAl}_2\text{O}_4$ /MgO interface by long-range diffusion. At the  $\text{MgAl}_2\text{O}_4$ /MgO dislocation-free interface segments, the oxygen sublattices of the two phases are almost identical, and transitioning between them only involves subtle shifts in atomic positions, retaining an almost identical densely packed oxygen fcc structure. Therefore the oxygen sublattices can be considered to be continuous from MgO to  $\text{MgAl}_2\text{O}_4$  and the structure transformation only requires exchange of  $\text{Al}^{3+}$  for  $\text{Mg}^{2+}$ . The stoichiometric equation for the MgO to  $\text{MgAl}_2\text{O}_4$  transformation is given in equation (1).

A comparison of the atomic structures between MgO and  $\text{MgAl}_2\text{O}_4$  at similar magnification (Figure 10) clearly shows that the oxygen lattices are largely maintained during transformation from MgO to  $\text{MgAl}_2\text{O}_4$ , while two full Mg atomic sites are replaced by two Al atoms, and one Mg is shifted from its original site to the center of one oxygen tetrahedron. The  $\text{MgAl}_2\text{O}_4$  cell shown here is only 1/8 of the smallest periodic unit cell, but the situation in the other 7/8 of the unit cell is similar, the Mg atom simply occupies different but equivalent oxygen tetrahedron centers.

The necessary exchange of cations is assumed to be energetically easy, which makes the dislocation-free portions of the  $\text{MgAl}_2\text{O}_4$ /MgO interface relatively mobile. In contrast,

movement of the misfit dislocations located at the intersection of about every 23rd (100) and (010)  $\text{MgAl}_2\text{O}_4$  plane with the interface can only occur by dislocation climb. This requires supply of not only  $\text{Mg}^{2+}$  and  $\text{Al}^{3+}$  cations but also oxygen. As the interface is largely coherent, there are very few possible oxygen sources.  $\text{Mg}^{2+}$  and  $\text{O}^{2-}$  could potentially be supplied by creating Schottky defects in reactant  $\text{MgO}$ , with  $\text{Al}^{3+}$  supplied by long range diffusion. Alternatively the necessary oxygen could be derived by forming non-stoichiometric  $\text{MgAl}_2\text{O}_4$ , with oxygen vacancies created (Schottky defects in  $\text{MgAl}_2\text{O}_4$ ).

Irrespective of the nature of the local source for oxygen, we hypothesize that climb of the misfit dislocations is comparatively difficult, requiring higher activation energies than cation exchange. As a consequence, propagation of the misfit dislocations - the extra (100) and (010) planes in  $\text{MgAl}_2\text{O}_4$  - lags behind during interface migration. The observed interface geometry with cusps pointing back into  $\text{MgAl}_2\text{O}_4$  at misfit dislocations suggests the propagation and climb of these extra  $\text{MgAl}_2\text{O}_4$  planes occurs by pull of the propagating dislocation-free sections of the interface. The jump in the chemical potential of  $\text{Mg}^{2+}$  associated with the  $\text{MgO}$  to  $\text{MgAl}_2\text{O}_4$  transformation provides a local driving force for interface motion. This corresponds to a pressure acting on the interface and pushing it into the reactant  $\text{MgO}$ . The misfit dislocations lag behind but due to surface tensions effects remain attached to the interface, similar to “Zener pinning”, where a second phase particle is dragged along by a moving interface [30]. The resulting scalloped shape and, in particular, the amplitude of the scalloped pattern reflect a stationary equilibrium of capillary forces at the intersections of the extra  $\text{MgAl}_2\text{O}_4$  lattice planes and the interface.

#### ***4.3 Formation of pores and domed configuration at interface on the $\mu\text{m}$ -scale.***

Oxygen diffusion required for dislocation climb is probably associated with the formation of Schottky defects, which introduce  $\text{Mg}^{2+}$  and  $\text{O}^{2-}$  vacancies into the precursor  $\text{MgO}$ . At the

dislocation-free portions of the interface the  $\text{MgAl}_2\text{O}_4$  (100) and (010) lattice planes are perfectly continuous across the interface. There are thus no dangling bonds or discontinuities in the oxygen sublattice that could serve as sinks for these vacancies. As a consequence, vacancies are expected to accumulate and transfer along the  $\text{MgAl}_2\text{O}_4$  GBs. The vacancies finally form pores at the junctions between  $\text{MgAl}_2\text{O}_4$  GBs and the  $\text{MgAl}_2\text{O}_4/\text{MgO}$  interface (see Figure 5), which also need to be dragged along with the migrating interface. Pore movement requires material transfer from the leading to the trailing edge of the pore, which most likely occurs by diffusion along the surface of the pore. The pores have finite mobility, thus pin the interface locally giving rise to the domed structure on the scale of individual grains (Figure 5).

This interpretation is corroborated by the finding shown in Figure 4. The voids only exist in the topotaxial part of the  $\text{MgAl}_2\text{O}_4/\text{MgO}$  interface, and are absent in the incoherent part. This is because in the incoherent part of the interface oxygen lattices are not continuous from  $\text{MgO}$  to  $\text{MgAl}_2\text{O}_4$ , and the incoherent  $\text{MgAl}_2\text{O}_4/\text{MgO}$  interface can behave as a natural oxygen vacancy sink.

The interface shows a non-planar geometry on both the nm-scale and the  $\mu\text{m}$ -scale. Both are due to the balance between the forces driving interface migration and the forces slowing it down. The defects which limit the interface mobility at different scales are different: misfit dislocations at the nm-scale, and pores at the  $\mu\text{m}$ -scale. However, the formation mechanism of the pores on the  $\mu\text{m}$ -scale is related to the climb of misfit dislocations at the nm-scale.

#### ***4.4 Discussion of the small misorientation between $\text{MgO}$ and $\text{MgAl}_2\text{O}_4$ grains***

Sieber et al. [24,31] observed similar misorientation angles at  $\text{MgAl}_2\text{O}_4/\text{MgO}$  interfaces to those found in this study, but with a  $2^\circ$  rotation around the [001] direction (perpendicular to

the interface), which is different to our result showing all misorientation axes in the plane of the interface. It is not clear what the reason is for the existence of a  $2^{\circ}$ - $4^{\circ}$  tilt of  $\text{MgAl}_2\text{O}_4$  (sub)grains with respect to MgO in our experiments, but it does help to reduce the lattice mismatch from -4.3% to -4.2%, and therefore slightly lowers the interfacial energy. It is possible that this misorientation is caused by the stress from uniaxial loading during sample growth.

## 5. Conclusion:

$\text{MgAl}_2\text{O}_4$  has been grown between MgO and  $\text{Al}_2\text{O}_3$  under high temperature and pressure. EBSD results show a topotaxial relationship at the  $\text{MgAl}_2\text{O}_4/\text{MgO}$  interface, with a small misorientation of  $\text{MgAl}_2\text{O}_4$  of  $2\sim 4^{\circ}$  around misorientation axes in the interface plane. Low-magnification STEM images show that  $\text{MgAl}_2\text{O}_4$  grains propagate into MgO with a domed interface geometry on the  $\mu\text{m}$ -scale. Zooming in to the atomic scale, a scalloped-shape interface structure has been found: periodical convex interface segments propagating towards MgO, with misfit dislocations located in the cusps with a  $\sim 4.5$  nm spacing. Theoretically, to accommodate the -4.2% lattice mismatch at the  $\text{MgAl}_2\text{O}_4/\text{MgO}$  interface requires one dislocation per 23-24 atomic planes in both [100] and [010] directions, which was indeed observed experimentally at the heads of domes. Observations of two different  $\text{MgAl}_2\text{O}_4$  grains at the interface, which show equivalent orientation relationships with MgO but with a  $90^{\circ}$  rotation to each other, are used to reconstruct the 3D interface configuration: the interface geometry reflects a grid of  $\text{MgAl}_2\text{O}_4$  lobate protrusions into MgO. A misfit dislocation is located at each cusp between the protrusions due to the occurrence of an extra  $\text{MgAl}_2\text{O}_4$  lattice plane.

The interface configuration at the nm-scale allows us to infer the interface migration mechanism: a balance is reached between the driving force of new phase growth and the

resistance to migration caused by climb of misfit dislocations. Due to the energy required for dislocation climb, the misfit dislocations pin the interface during progressive phase transformation. Furthermore, because extra oxygen atoms are required for the climb of misfit dislocations, interface migration generates many oxygen vacancies that accumulate at the topotaxial interface, forming pores. The pores control the  $\mu\text{m}$ -scale development of the interface shape by also behaving as pins during interface propagation. Fundamental understanding of the interface reaction and migration on the atomic scale is the key to understanding the interface migration on the  $\mu\text{m}$ -scale. This understanding, and the strategy of combining the study of structure on the atomic- and  $\mu\text{m}$ -scale, should help to understand the interface structure of a wide range of materials.

### **Acknowledgement:**

This research was funded by the European Union's Horizon 2020 research and innovation programme under the Marie Skłodowska-Curie grants No. 656378 – Interfacial Reactions (CL) & No. 655760 – Digiphase (TJP), and the Austrian Science Fund (FWF): I1704-N19 in the framework of the research group FOR741-DACH (GH). The FEI Quanta 3D FEG-SEM instrument is supported by the Faculty of Geosciences, Geography and Astronomy at the University of Vienna (Austria), and the Nion UltraSTEM is supported by the Faculty of Physics, University of Vienna (Austria).

### **References:**

- [1] H. J. Fan, M. Knez, R. Scholz, K. Nielsch, E. Pippel, D. Hesse, M. Zacharias, and U. Gösele, *Nat. Mater.*, 5 (2006), p. 627.
- [2] H. J. Fan, U. Gösele, and M. Zacharias, *Small*, 3 (2007), p. 1660.
- [3] C. Li, J. Poplawsky, N. Paudel, T.J. Pennycook, S.J. Haigh, M.M. Al-Jassim, Y. Yan, and S.J. Pennycook, *IEEE J. Photovoltaics*, 4 (2014), p. 1636.
- [4] D. Hesse, *J. Vac. Sci. Technol. A*, 5 (1987), p. 1696.
- [5] P. Pitra, A.N. Kouamelan, M. Ballevre, and J.-J. Peucat, *Journal of Metamorphic Geology*, 28 (2010), p. 41.
- [6] R. Joesten, and G. Fisher, *Geological Society of America Bulletin*, 100 (1988), p. 714.

- [7] L.M. Keller, R. Abart, R. Wirth, D.W. Schmid, and K. Kunze, *American Mineralogist*, 91 (2006), p. 1024.
- [8] L.M. Keller, R. Wirth, D. Rhede, K. Kunze, and R. Abart, *Journal of Metamorphic Geology*, 26 (2008), p. 99.
- [9] R.H. Vernon, *A Practical Guide to Rock Microstructure*, Cambridge University Press, 2004.
- [10] C.B. Carter, and H. Schmalzried, *Philos. Mag. A*, 52 (1985), p. 207.
- [11] D. Hesse, H. Sieber, P. Werner, R. Hillebrand, and J. Heydenreich, *Zeitschrift Für Physikalische Chemie*, 187 (1994), p. 161.
- [12] D.X. Li, P. Pirouz, A.H. Heuer, S. Yadavalli, and C.P. Flynn, *Philos. Mag. A*, 65 (1992), p. 403.
- [13] L.C. Götze, R. Abart, E. Rybacki, L.M. Keller, E. Petrishcheva, and G. Dresen, *Miner Petrol*, 99 (2009), p. 263.
- [14] L.C. Götze, R. Abart, R. Milke, S. Schorr, I. Zizak, R. Dohmen, and R. Wirth, *Phys Chem Minerals*, 41 (2014), p. 681.
- [15] P. Jeřábek, R. Abart, E. Rybacki, and G. Habler, *American Journal of Science*, 314 (2014), p. 940.
- [16] L.M. Keller, L.C. Gotze, E. Rybacki, G. Dresen, and R. Abart, *American Mineralogist*, 95 (2010), p. 1399.
- [17] E.B. Watson, and J.D. Price, *Geochimica Et Cosmochimica Acta*, 66 (2002), p. 2123.
- [18] R.C. Rossi, and R.M. Fulrath, *Journal of the American Ceramic Society*, 46 (1963), p. 145.
- [19] D. Hesse, S.T. Senz, R. Scholz, P. Werner, and J. Heydenreich, *Interface Science*, 2 (1994), p. 221.
- [20] E. Koch, and C. Wagner, *Zeitschrift Für Physikalische Chemie*, 34 (1936), p. 317.
- [21] W.P. Whitney II, and V.S. Stubican, *Journal of Physics and Chemistry of Solids*, 32 (1971), p. 305.
- [22] R. Abart, J. Svoboda, P. Jeřábek, E. Povoden-Karadeniz, and G. Habler, *American Journal of Science*, 316 (2016), p. 309.
- [23] H. Sieber, D. Hesse, P. Werner, and S. Senz, *Defect and Diffusion Forum Vols*, 143-147 (1997), p. 649.
- [24] H. Sieber, D. Hess, and P. Werner, *Philos. Mag. A*, 75 (1997), p. 889.
- [25] H. Sieber, P. Werner, and D. Hesse, *Philos. Mag. A*, 75 (1997), p. 909.
- [26] F. Bachmann, R. Hielscher, and H. Schaeben, *Ssp*, 160 (2010), p. 63.
- [27] R. Hielscher, H. Schaeben, and H. Siemes, *Math Geosci*, 42 (2010), p. 359.
- [28] P.P. Dholabhai, G. Pilania, J.A. Aguiar, A. Misra, and B.P. Uberuaga, *Nat. Commun*, 5 (2014), p. 1.
- [29] W. Bollmann, *Crystal Defects and Crystalline Interfaces*, Springer Berlin Heidelberg, 1970.
- [30] E. Nes, N. Ryum, and O. Hunderi, *Acta Metallurgica*, 33 (1985), p. 11.

[31] H. Sieber, D. Hesse, X. Pan, S. Senz, and J. Heydenreich, Zeitschrift Fur Anorganische Und Allgemeine Chemie, 622 (1996), p. 1658.

Figure Captions:

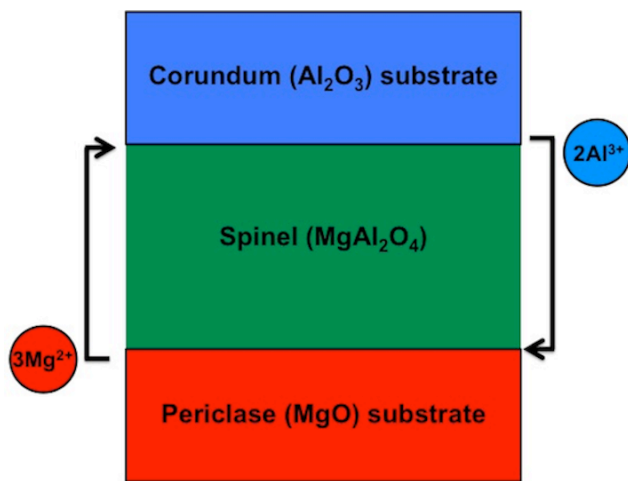


Figure 1. A sketch showing composition change during the growth of  $\text{MgAl}_2\text{O}_4$  spinel between  $\text{MgO}$  and  $\text{Al}_2\text{O}_3$ .

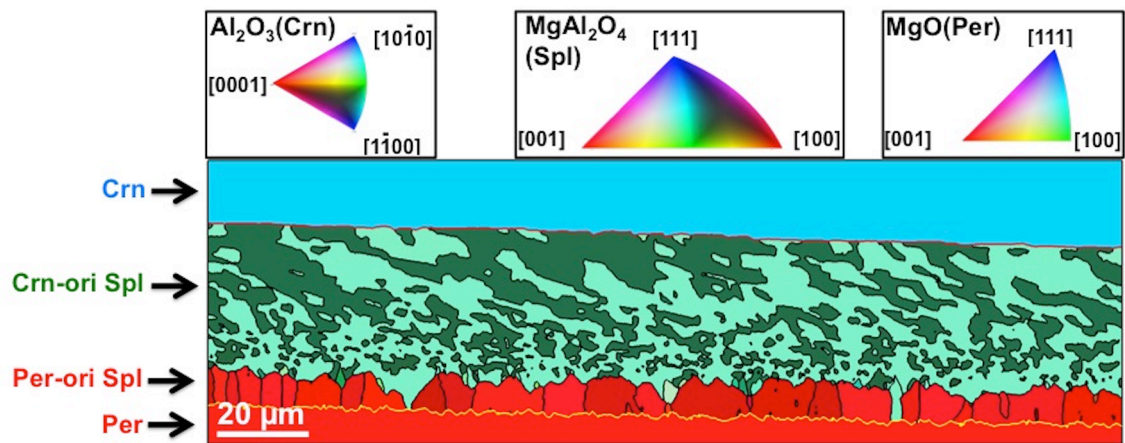


Figure 2. EBSD IPF map (reference vector in horizontal (x) direction) of reconstructed grains showing corundum (blue), periclase (red) and two layers of  $\text{MgAl}_2\text{O}_4$  spinel: Crn-ori Spl including twin structure (dark and light green), and Per-ori Spl (red). Boundaries with  $> 2^\circ$  misorientation angle are shown as black lines. The  $\text{MgAl}_2\text{O}_4/\text{MgO}$  interface is marked in yellow, the  $\text{Al}_2\text{O}_3/\text{MgAl}_2\text{O}_4$  interface in red. To show twins, spinel IPF color coding uses only the purely rotational part of the Laue group symmetry.



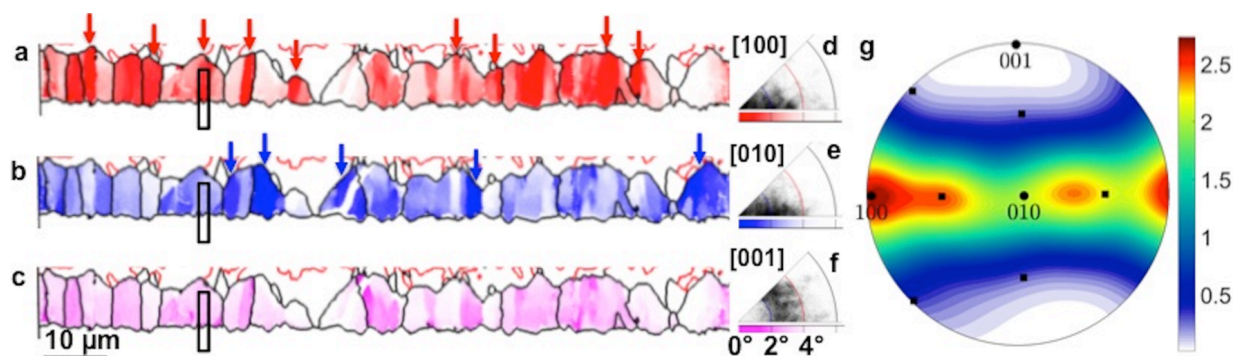


Figure 3. EBSD crystallographic orientation mapping (a-c) and corresponding inverse pole figures (IPFs) (d-f) show orientation deviation of the  $\text{MgAl}_2\text{O}_4$  grains with respect to MgO substrate along the three MgO  $\langle 100 \rangle$  directions. Grain boundaries are defined by point to point lattice misorientations of  $> 2^\circ$ , marked by dark lines on maps. Most of the  $\text{MgAl}_2\text{O}_4$  grains are tilted  $2^\circ$ - $4^\circ$  away from the [001] axis of MgO, and  $0^\circ$ - $4^\circ$  for [100] and [010] axes. Colors from dark to light in the EBSD maps indicate orientation deviation angle from  $0^\circ$  to  $4^\circ$ . The red and blue arrows point to the  $\text{MgAl}_2\text{O}_4$  grains (and sub-grains) with close orientation with [100] or [010] axes of MgO, respectively. The black boxes mark the position where the FIB specimen was extracted. Part (g) is an equal area upper hemisphere plot of the misorientation axes between Per-ori Spl and MgO for the map in this figure. The plot is smoothed using a halfwidth of  $18^\circ$  (chosen to approximate the calculated MO axis error) and contoured for multiples of the uniform distribution (see colorbar). MgO  $\langle 100 \rangle$  directions are plotted as black circles, and  $\langle 110 \rangle$  directions as black squares.

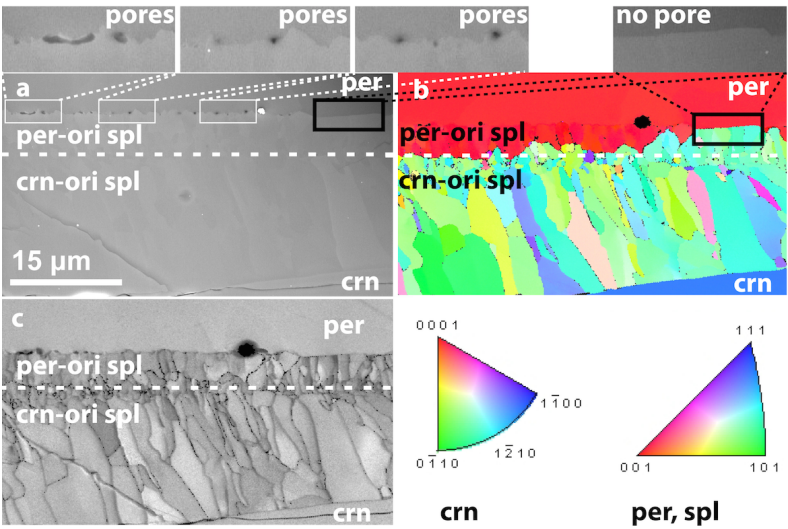


Figure 4. (a) SEM image of  $\text{MgAl}_2\text{O}_4$  spinel (Spl) interlayer between  $\text{MgO}$  periclase (Per) and  $\text{Al}_2\text{O}_3$  corundum (Crn) reactants. The horizontal dashed white line indicates the position of original periclase-corundum contact. Higher-magnification inner images show that pores exist at the interface areas marked by white boxes, but not in the rightmost area marked by a black box. (b) Inverse pole figure map shows most of the spinel-periclase interface has a topotactic orientation relationship, only the rightmost area without pores shows no special orientation relationship, where corundum-oriented spinel builds up the entire spinel interlayer. (c) EBSD image quality map showing internal microstructure.

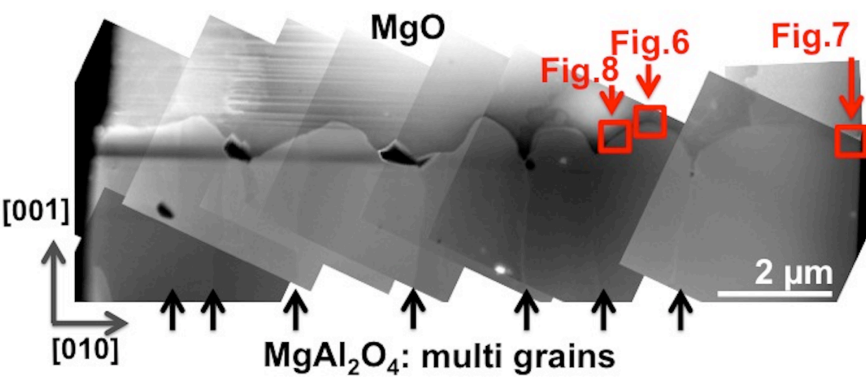


Figure 5. A group of HAADF images showing an overview of the entire FIB specimen (location of the specimen marked in Figure 3). The red boxes mark the positions where high resolution images in Figures 6-8 were taken.

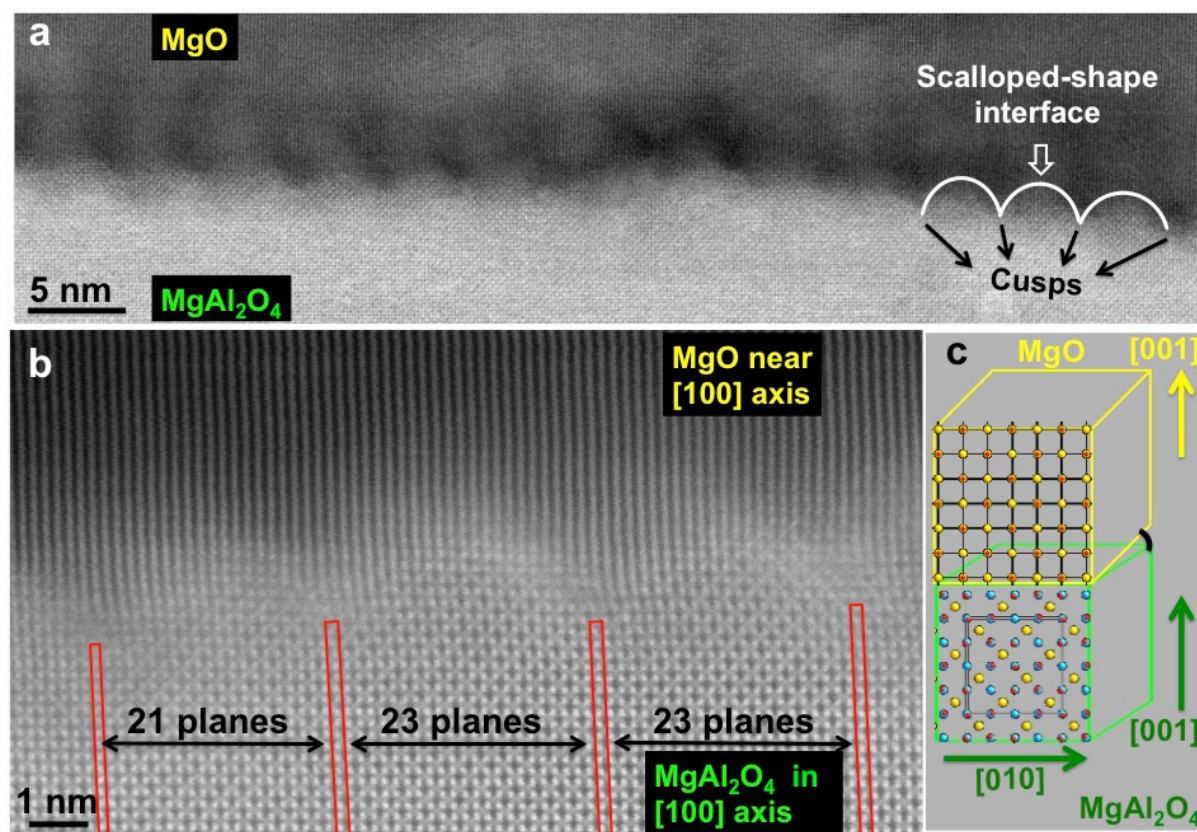


Figure 6. (a) STEM image shows a scalloped-shape MgAl<sub>2</sub>O<sub>4</sub>/MgO interface formed by periodic MgAl<sub>2</sub>O<sub>4</sub> curved segments which convex towards MgO, and cusps between the segments at interface. (b) Periodic misfit dislocations at the cusps position on the interface, with  $\sim 4.5$  nm spacing. The red boxes indicate extra MgAl<sub>2</sub>O<sub>4</sub> planes. (c) Sketch shows the orientation relationship between MgAl<sub>2</sub>O<sub>4</sub> and MgO, where the yellow, blue and red circles indicate Mg, Al and O atoms, respectively.



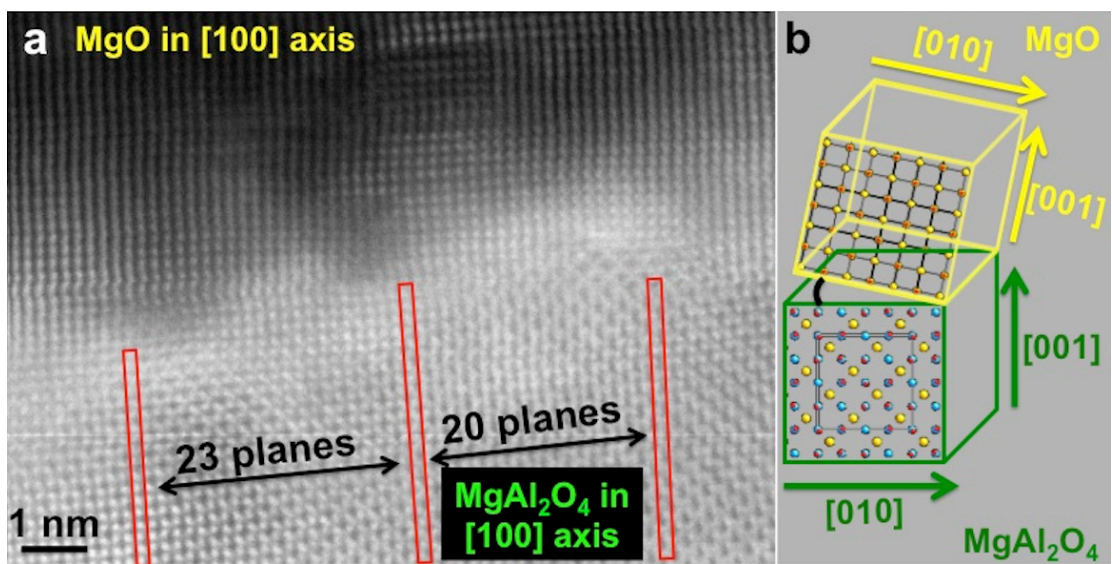


Figure 7. (a) STEM image shows scalloped-shape MgAl<sub>2</sub>O<sub>4</sub>/MgO interface with misfit dislocations at the cusps position, on an interface section with a different orientation relationship drawn by a sketch in (b). The red boxes in (a) indicate extra MgAl<sub>2</sub>O<sub>4</sub> planes. The yellow, blue and red circles in the sketch indicate Mg, Al and O atoms, respectively.

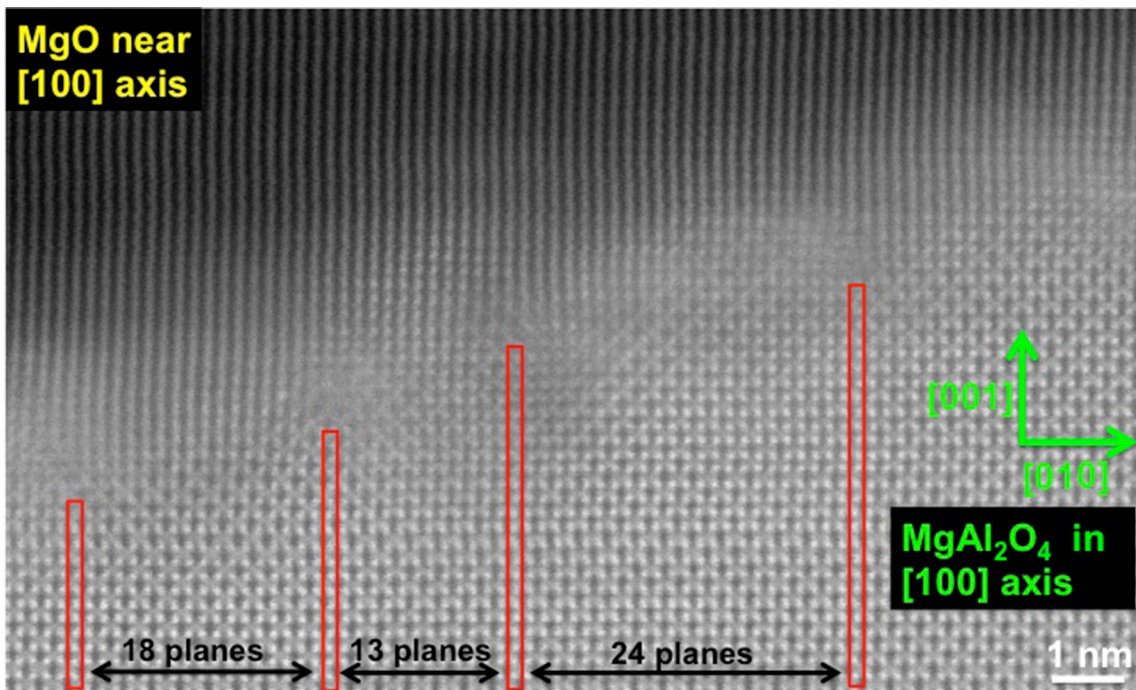


Figure 8. Periodic scalloped-shape MgAl<sub>2</sub>O<sub>4</sub>/MgO interface at an inclined section, where the spacings between dislocations are less regular and usually smaller than those at the flat interface area. The red boxes indicate extra MgAl<sub>2</sub>O<sub>4</sub> planes.

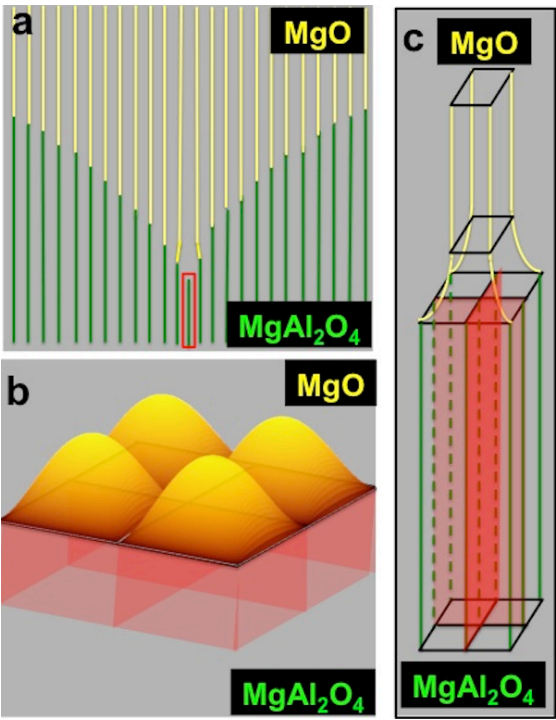


Figure 9. (a) 2D schematic model showing an extra plane (red box) in  $\text{MgAl}_2\text{O}_4$ , forming a misfit dislocation at the “cusp” position on the scalloped-shape interface. (b) 3D schematic model showing that the misfit dislocations in  $\text{MgAl}_2\text{O}_4$  and the periodic convex interface segments form supercells, with a lattice parameter of  $\sim 4.5$  nm. (c) A detailed view shows that at the joint of supercells, three  $\text{MgAl}_2\text{O}_4$  planes merge into two  $\text{MgO}$  planes along both  $[100]$  and  $[010]$  directions. The red planes indicate extra  $\text{MgAl}_2\text{O}_4$  planes.

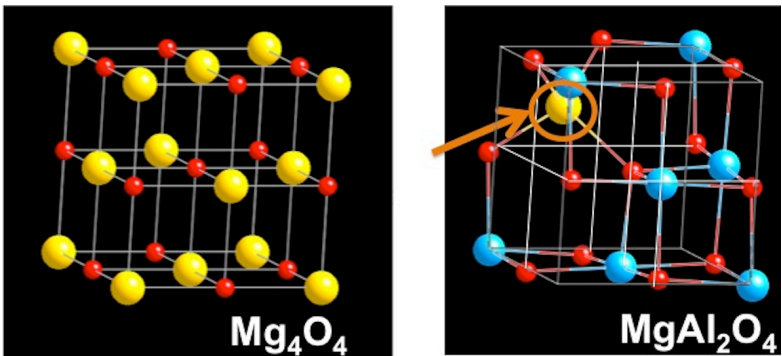


Figure 10. Atomic structure comparison between  $\text{MgO}$  and  $\text{MgAl}_2\text{O}_4$  at similar magnification. Four  $\text{MgO}$  unit cells and  $1/8$  of a  $\text{MgAl}_2\text{O}_4$  cell are shown. The oxygen (red) lattices maintain similarity during transformation from  $\text{MgO}$  to  $\text{MgAl}_2\text{O}_4$ , while two Mg (yellow) atomic sites have been replaced by two Al (blue) atoms and one Mg has shifted from the original site to the centre of one oxygen-tetrahedron (indicated by orange arrow).